Materials Technology Reports 2026, 4(1), 3955.
doi: https://doi.org/10.59400/mtr3955

Article

Exploring the effect of graphite-coating on hexanary high entropy metal oxides towards efficient water electrocatalysis

Shakeel Abbas[1], Akbar Hussain[1], Muhammad Asim[1,*], Tehmeena Maryum Butt[1], Banafsha Habib Ur Rehman[1], Javeria Arshad[1], Amina Hana[1], Sadia Kanwal[1], Muhammad Yasir[2], Naveed Kausar Janjua[1,*]

[1] Department of Chemistry, Quaid-i-Azam University, Islamabad 45320, Pakistan
[2] Department of Material Science and Engineering, Institute of Space Technology, Islamabad 44000, Pakistan
*** Corresponding author:** Muhammad Asim, masim@chem.qau.edu.pk or nkausarjanjua@yahoo.com; Naveed Kausar Janjua, nkjanjua@qau.edu.pk

CITATION

Abbas S, Hussain A, Asim M, et al. Exploring the effect of graphite-coating on hexanary high entropy metal oxides towards efficient water electrocatalysis. Materials Technology Reports. 2026; 4(1): 3955. https://doi.org/10.59400/mtr3955

ARTICLE INFO

Received: 26 January 2026
Revised: 23 February 2026
Accepted: 27 February 2026
Available online: 6 March 2026

Abstract: High-entropy oxides (HEOs) have emerged as promising electrocatalysts due to their high configurational entropy, modular electronic structures, and defect-rich multicationic lattices. However, modifying their electrochemical kinetics through conductive surface modification remains completely unknown. An Al-rich hexanary spinel, Cr, Cd, Fe, Mg, and Mn-based materials were synthesized using a sol-gel method and then modified with graphite (5–20 wt%) via rotary ball milling to improve conductivity and interfacial charge transfer, resulting in a stable spinel phase as validated by Rietveld-refined XRD. The addition of graphite significantly increased anodic activity, with the 10 wt% composite (HEO-10C) achieving a peak current density of 47.09 mA cm^{-2} in 1 M KOH + methanol. This was followed by decreased charge-transfer resistance and better electron-transfer kinetics. The graphite-HEO interface allows for faster reaction pathways, as evidenced by a high diffusion coefficient (8.65×10^{-8} cm^2 s^{-1}), a heterogeneous electron-transfer rate constant (3.75×10^{-4} cm s^{-1}), and a low Tafel slope of 97 mV dec^{-1}. To better measure intrinsic activity, we add a new descriptor, $J\eta$ = (J_p (peak current density)−J_{onset} (onset current density)), which represents the net operating current above onset. $J\eta$ correlates strongly with traditional kinetic measurements, highlighting the conductivity-driven performance gain in HEO-10C (44.59 mA cm^{-2}), which is about 1.6× greater than the uncoated HEO. These findings confirm graphite coating as a viable method for modifying multication HEO electrodynamics and introduce a new measure for assessing advanced oxide-based electrocatalysts.

Keywords: water electrocatalysis; high entropy oxides; graphite coating; low charge transfer resistances; robust kinetics

1. Introduction

The increasing worldwide energy demand, driven by rapid industrialization, urban development, and population increase, has put further strain on traditional energy systems. Fossil fuels continue to meet a significant portion of global energy demand, leading to greenhouse gas buildup, air pollution, water shortages, and ecosystem degradation [1–3]. The continued use of carbon-intensive fuels has directly led to global climate instability, resulting in rising temperatures, desertification, glacier melt, and an alarming increase in the frequency of extreme weather events such as floods, droughts, and cyclones. These compounding issues highlighted the need to move to more sustainable, environmentally friendly, and carbon-neutral energy conversion routes [4].

Electrochemical energy technologies such as fuel cell devices, water electrolyzers, metal-air batteries, and unitized regenerative systems have emerged as prominent options due to their high energy density, modularity, and minimal environmental effect [5–7]. Their widespread use, however, is dependent on the development of strong electrocatalysts capable of speeding oxygen/hydrogen redox kinetics with high efficiency, durability, and cost-effectiveness. Noble metal catalysts like Pt, IrO_2, and RuO_2 set the standard for HER, OER, and ORR. However, their scarcity, price, and sensitivity to performance degradation under operating settings severely restrict their viability for wider commercialization [8, 9]. These limits have driven research into earth-abundant, multifunctional, and structurally tailored electrocatalysts suited for OER, HER, and ORR in alkaline conditions.

Amongst renewable energy options, electrochemical water splitting consists of two kinetically slow half-reactions: the oxygen evolution reaction (OER) at the anode and the hydrogen evolution reaction (HER) at the cathode, both of which need active electrocatalysts to overcome significant overpotentials and critical reaction barriers. Monofunctional and bifunctional electrocatalysts have been extensively studied; yet, attaining high catalytic activity, long-term stability, quick electron transport, and structural robustness while scaling water splitting technologies remains a major challenge [10–12].

The introduction of high-entropy oxides (HEOs) represents a paradigm shift in catalyst design. HEOs, which were first described by Rost et al. [13], make use of a multi-cation lattice with high configurational entropy to stabilize metastable phases and create an extraordinarily adjustable electronic structure. The configurational entropy of these systems, computed using Equation (1), originates mostly from the cationic distribution, given the minimal entropic contribution of anions [14].

$$\mathrm{S_{config}} = \left[\left(\sum\nolimits_{i=1}^{N} x_i ln x_i\right)_{\text{cation-site}} + \left(\sum\nolimits_{j=1}^{M} x_j ln x_j\right)_{\text{anion-site}}\right] \tag{1}$$

where R is the universal gas constant, and x_i and x_j stand for the mole fractions of the elements found in the cation and anion sites, respectively. Since the entropy input from oxygen ions is about zero by one mole fraction, the cationic contribution accounts for all of the entropy. This entropy-driven stabilization results in distinct defect chemistries, variable oxidation states, lattice distortions, and improved ionic/electronic transport-all of which are extremely favourable for electrocatalytic applications. In recent years, HEOs with spinel, rock-salt, perovskite, and fluorite structures have shown outstanding performance metrics for OER, HER, and ORR, frequently outdoing or exceeding noble-metal standards [15,16].

The catalytic potential of high-entropy oxides (HEOs) for oxygen evolution reaction (OER) applications is highlighted by a growing number of recent studies [12, 17]. According to He et al., $FeCoNiCrMn_3O_4$ combined with hollow carbon spheres achieved exceptional structural stability and an astonishingly low overpotential of 263 mV [18]. By creating a compositionally complex $(Cr_{0.2}Mn_{0.2}Fe_{0.2}Ni_{0.2}Zn_{0.2})_3O_4$ structure that preserved excellent lattice resilience and produced an overpotential of 295 mV, Yang et al. further illustrated the potential of multicomponent spinels [19]. In support of these findings, Wang et al. produced $CoCuFeMnNi_3O_4$/MWCNT hybrids with an overpotential of 350 mV and faster charge-transfer kinetics [20]. By creating MOOH nanosheets in situ on $(CoNiMnZnFe)_3O_{3.2}$, Zhang et al. advanced this field and produced a highly active core–shell shape with an overpotential of 336 mV [21]. Our own earlier research showed that microwave-assisted synthesis of HEOs greatly increased OER activity, producing overpotentials as low as 350 mV and preserving outstanding structural robustness under working conditions [22].

These developments highlight the versatility of HEOs, but there are still two major limitations: first, because oxide phases predominate, their intrinsic electronic conductivity is frequently insufficient; and second, particle agglomeration or poorly designed interfacial architectures can limit the accessibility and utilization of catalytic surface sites. To fully harness the catalytic potential of HEO-based systems, these enduring issues require purposeful material change, especially through conductive carbon integration and interface engineering [23,24].

To address these constraints, carbon-based conductive interfaces have proven to be a highly effective strategy. Charge transfer kinetics are accelerated, and durability is improved by the high electrical conductivity, strong interfacial bonding, vast surface area, and superior chemical stability of carbon materials, along with graphene, carbon nanotubes, amorphous carbon, and graphite [25]. There is mounting evidence that HEO-carbon composites and carbon-coated HEOs have significantly increased electrocatalytic activity because of synergistic actions that alter electronic states, stabilize surface intermediates, and prevent lattice breakdown during cycling. In comparison to pure HEOs, many recent papers show that carbon-modified HEO composites produce better OER/HER kinetics, lower overpotentials, and greater lifespans [26–28].

In this study, we carefully designed carbon-coated high-entropy oxides (HEO-xC) to take advantage of both conductive carbon interface and high-entropy configurational tailoring. The conformal carbon coating carries out several mechanistic tasks, including: (1) introducing oxygen-rich functional groups that modulate adsorption energetics; (2) improving electrical conductivity, which facilitates quick electron transport; (3) creating a protective structural matrix that enhances chemical and mechanical stability; and (4) creating a core-shell morphology that maximizes electroactive surface area. With an enhanced heterogeneous electron transfer rate constant ($k_0 = 3.75 \times 10^{-1}$ cm s^{-1}), a high diffusion coefficient ($D_0 = 8.65 \times 10^{-1}$ cm^2 s^{-1}), and a favourable Tafel slope of 97 mV dec^{-1}, the resultant HEO-10C catalyst has markedly improved electrochemical kinetics. The efficacy of graphite-based interfacial engineering is demonstrated in the current work, where the Jη descriptor shows that HEO-10C provides a 1.6-fold increase in catalytic activity over its uncoated equivalent.

Current work establishes carbon-coated HEOs as a potential new class of high-performance, structurally customizable, earth-abundant electrocatalysts.

HEO-xC provides a scalable route toward next-generation oxygen evolution catalysts that can enable sustainable electrochemical energy technologies and renewable hydrogen production by fusing high-entropy lattice engineering with conductive carbon topologies.

2. Materials and method

2.1. Materials

Aluminum nitrate nonahydrate ($Al(NO_3)_3 \cdot 9H_2O$), magnesium nitrate hexahydrate ($Mg(NO_3)_2 \cdot 6H_2O$), iron(III) nitrate nonahydrate ($Fe(NO_3)_3 \cdot 9H_2O$), cadmium nitrate tetrahydrate ($Cd(NO_3)_2 \cdot 4H_2O$), chromium(III) nitrate nonahydrate ($Cr(NO_3)_3 \cdot 9H_2O$), manganese(II) nitrate tetrahydrate ($Mn(NO_3)_2 \cdot 4H_2O$), ammonium hydroxide (NH_4OH), citric acid ($C_6H_8O_7$), potassium hydroxide (KOH), ethanol (C_2H_5OH), and methanol (CH_3OH). Nafion (5 wt% in lower aliphatic alcohols/H_2O) was used as a binder, and Graphite powder (Purity: $\geq 99.99\%$) was used as a carbon source. All the chemicals were used as received without any additional treatment.

2.2. Synthesis procedure for high entropy oxide

HEOs were synthesized through an optimized sol-gel route followed by graphite coating via ball-milling. This combined methodology provides several advantages: (1) excellent phase purity, (2) energy-efficient processing conditions, and (3) precise control over material morphology. For the sol-gel synthesis, stoichiometric amounts of metal precursors (0.35 M for Al and 0.25 M for other cations) were sequentially dissolved in deionized water under continuous magnetic stirring (500 rpm) to achieve molecular-level homogeneity. Citric acid (1.5:1 molar ratio relative to total metal ions) was introduced as a complexing agent, yielding a uniform sol. The pH was carefully adjusted to 7.0 ± 0.1 through controlled addition of ammonium hydroxide (1 M) while maintaining vigorous stirring (800 rpm) to prevent localized precipitation. The homogeneous sol was subsequently converted to a gel by heating at 120 °C for 12 h with constant mechanical agitation, ensuring uniform solvent evaporation while preventing particle agglomeration. After aging at room temperature for 24 h, the xerogel was calcined at 800 °C for 7 h (heating rate: 5 °C min^{-1}) in air to crystallize the single-phase HEO, which was then mortar-ground to a fine powder (particle size < 50 μm).

2.3. Synthesis of graphite-coated high entropy oxides (HEO-xC)

The graphite coating was applied to the high-entropy oxide (HEO) through a controlled rotary ball-milling process. Precise graphite loadings (5–20 wt%) were achieved by mixing stoichiometric quantities of HEO with graphite powder in acetone (20 mL solvent per gram of solids) using zirconia milling media (ball-to-powder weight ratio = 4:1). Each composition underwent mechanical milling for 3 h at 300 rpm to ensure uniform carbon dispersion. Post-milling, the solvent was removed through controlled evaporation at 80 °C for 12 h under static air conditions, yielding homogeneous composite powders. This procedure was systematically repeated across all designed compositions, with the resulting specimens labeled HEO-xC (where x = 0, 5, 10, 15, and 20 wt% of graphite powder) and summarized in **Table 1**. The as-prepared graphite-HEO composites were subsequently characterized and evaluated for their physical and electrochemical properties.

Table 1. Composition, sample codes, average crystallite sizes, and EDS results of HEO-xC.

Composition/elements	**Code**	**D_{av} (nm) ±0.01**	**C (wt.%)**	**O (wt.%)**	**Mg (wt.%)**	**Al (wt.%)**	**Cr (wt.%)**	**Mn (wt.%)**	**Cd (wt.%)**	**Fe (wt.%)**
$[Al_{35}(CdCrFeMgMn)_{65}]_3O_4$	HEO	20.7	0	51.45	3.56	3.23	4.04	8.83	14.15	7.39
$[Al_{35}(CdCrFeMgMn)_{65}]_3O_4$-5C	HEO-5C	21.4	4.37	48.26	3.28	2.70	6.88	10.36	16.88	7.26
$[Al_{35}(CdCrFeMgMn)_{65}]_3O_4$-10C	HEO-10C	30.5	8.03	37.29	2.91	2.52	7.93	14.96	15.25	11.12
$[Al_{35}(CdCrFeMgMn)_{65}]_3O_4$-15C	HEO-15C	22.6	2.27	46.72	3.13	2.49	7.69	11.19	19.10	7.90
$[Al_{35}(CdCrFeMgMn)_{65}]_3O_4$-20C	HEO-20C	25.2	5.49	22.45	1.39	1.44	12.45	23.04	15.81	17.94

2.4. Electrode modification

Prior to modification, the glassy carbon electrode (GCE) undergoes systematic pretreatment to ensure a clean, reproducible surface. The electrode is sequentially polished with aqueous alumina slurry using a microcloth pad, followed by thorough rinsing with deionized water and HPLC-grade acetone to remove residual particulates and organic contaminants. For catalyst deposition, we employ a controlled drop-casting protocol: (1) the polished GCE is pre-wetted with 2 μL ethanol to enhance catalyst adhesion, (2) 0.1 mg of finely ground catalyst is deposited, and (3) 2 μL of 0.5% Nafion solution is applied as a polymeric binder. The modified electrode is subsequently cured at 45 °C for 30 min to ensure uniform film formation while preserving catalyst integrity.

2.5. Physical and electrochemical characterizations

The crystallographic properties of synthesized materials were characterized by X-ray diffraction (XRD) using a PANalytical Empyrean diffractometer with Cu Kα radiation (λ = 1.5406 Å). Measurements were performed in the 2θ range of 20–80° with a step size of 0.02° and scan rate of 0.02° s^{-1}. FTIR spectra for all the prepared HEOs were obtained in the wavelength range between 400–4000 cm^{-1} using a Nicolet 5PC instrument, where the samples were mixed with KBr powder. Morphological analysis and semi-quantitative elemental mapping were conducted using field-emission scanning electron microscopy with energy-dispersive X-ray spectroscopy (FE-SEM/EDX, Zeiss Sigma 300) operated at 15 kV accelerating voltage.

The electrochemical properties of the synthesized carbon-coated-HEOs were evaluated using a Gamry Interface 1010B potentiostat in a standard three-electrode configuration. The system comprised: a modified glassy carbon electrode as the working electrode, a Pt wire counter electrode, and an Ag/AgCl reference electrode (3 M KCl filling solution). All measurements were conducted in 1 M KOH with/without methanol at room temperature.

Cyclic voltammetry (CV) and linear sweep voltammetry (LSV) measurements were conducted in 1 M KOH electrolyte (pH 13.6) with and without methanol additive, employing scan rates ranging from 20 to 100 mV s^{-1}. Electrochemical impedance spectroscopy (EIS) measurements were performed using a sinusoidal potential perturbation with 10 mV amplitude, spanning frequencies from 0.1 Hz to 100 kHz (10 points per decade). The impedance response was recorded at multiple DC bias potentials corresponding to key electrochemical processes, with each measurement preceded by a 100 s open-circuit potential stabilization period. All potentials measured against the Ag/AgCl reference electrode (3 M KCl) were converted to the reversible hydrogen electrode (RHE) scale using the Nernst equation ($E_{RHE} = E_{Ag/AgCl} + 0.197 + 0.059*pH$). Key electrochemical parameters, including onset potential, overpotential at 10 mA cm^{-2}, Tafel slope, and impedance values, were derived from the measured data.

3. Results and discussion

3.1. Structural analysis

Figure 1a presents the X-ray diffraction patterns of the synthesized materials. The observed sharp diffraction peaks confirm the highly crystalline nature of the catalysts, while the absence of extraneous peaks indicates phase purity. All graphite-coated high-entropy oxides (HEO-xC) exhibit characteristic reflections consistent with a cubic spinel structure (space group $Fd\bar{3}m$), as evidenced by their precise alignment with the reference pattern shown in **Figure 1b** (JCPDS #22-1084) [29].

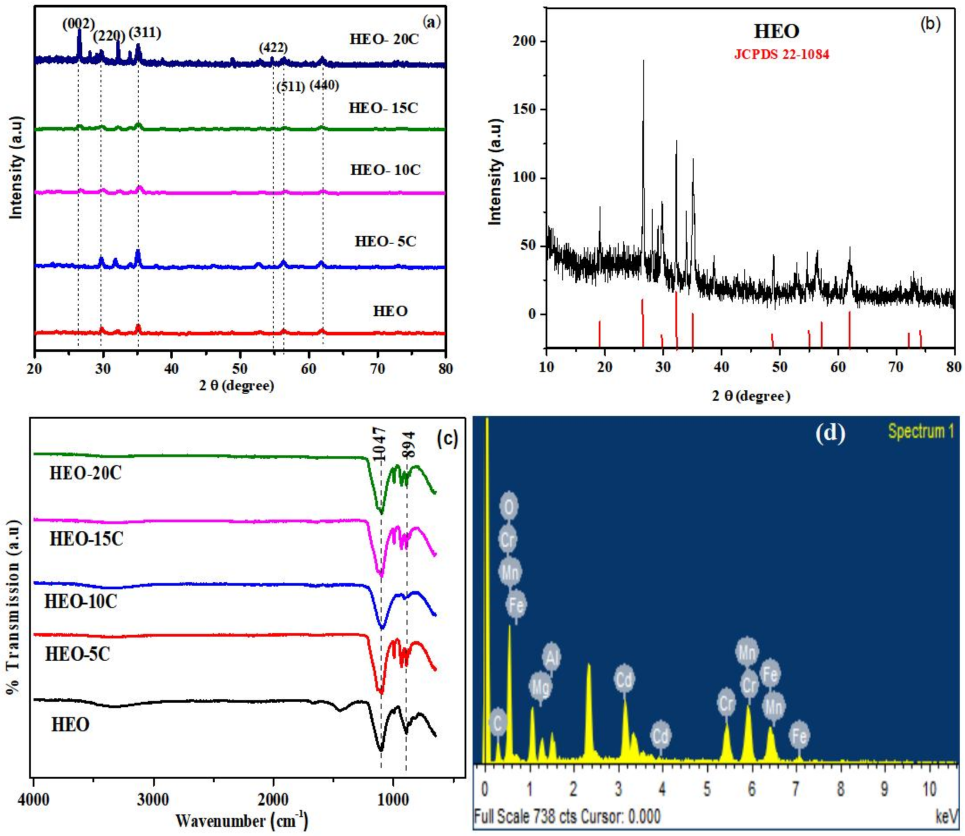

Figure 1. *Cont.*

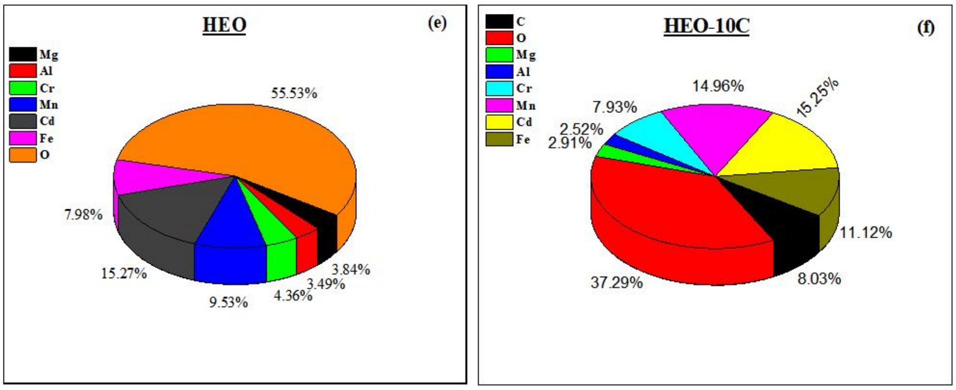

Figure 1. **(a)** XRD patterns; **(b)** XRD pattern comparison with JCPDS card; **(c)** FTIR spectra of synthesized HEO-xC; **(d)** EDX of HEO-10C, and EDX elemental composition Pi-chart for: **(e)** HEO; **(f)** HEO-10C.

From these XRD patterns, the average crystallite size of as-prepared graphite-coated high entropy oxides (HEO-xC) was calculated by using the Debye-Scherrer formula [30].

$$\mathrm{D_{av}}\ (\mathrm{nm}) = \frac{K\lambda}{\beta \cos \theta} \tag{2}$$

Where, D_{av} is the average crystallite size, K is the crystallite shape constant, and β is the diffraction peak width in radians. The D_{av} of the as-synthesized HEO-xC powders was in the 20 to 30 nm range and summarized in **Table 1**.

FTIR was employed to verify the metal-oxygen bonding characteristics and phase purity of the synthesized materials (**Figure 1c**). Spectra were acquired in transmission mode (400–4000 cm^{-1}) for the sintered HEOs/C composites. Two distinct vibrational regions were identified: (i) 400–700 cm^{-1} corresponding to ν(M-O) stretching modes at octahedral coordination sites, and (ii) 7000–1100 cm^{-1} representing tetrahedral-site ν(M-O) vibrations in the spinel lattice. The absence of absorption bands above 1100 cm^{-1} confirms the lack of organic residues or surface contaminants. These spectral features exhibit excellent agreement with reference data for cubic spinel oxides, further validating the phase purity and structural integrity of the HEO-xC system [31–33]. Additionally, no water-related peaks were detected in the FTIR spectrum. EDX analysis confirmed the presence of all expected elements, with the quantitative composition of each element listed in **Table 1**. Additionally, the EDX spectrum and weight percentage (wt%) pie chart for HEO and HEO-10C are presented in **Figure 1d–f**.

Scanning electron microscopy (SEM) analysis was carried out to study the surface morphology, elemental distribution, and homogeneity of the HEO-xC materials [34–36]. SEM analysis of the synthesized high-entropy oxide/carbon (HEO-xC) composites was conducted at 1 μm and 50 μm resolutions to evaluate their microstructural characteristics. As depicted in **Figures 2** and **3**, the materials exhibit a spongy, highly porous morphology with uniform distribution, suggesting an enhanced surface area and potential catalytic activity. This structural homogeneity, combined with the interconnected porous network, is conducive to facilitated mass transport and active site accessibility, which may contribute to improved electrocatalytic performance.

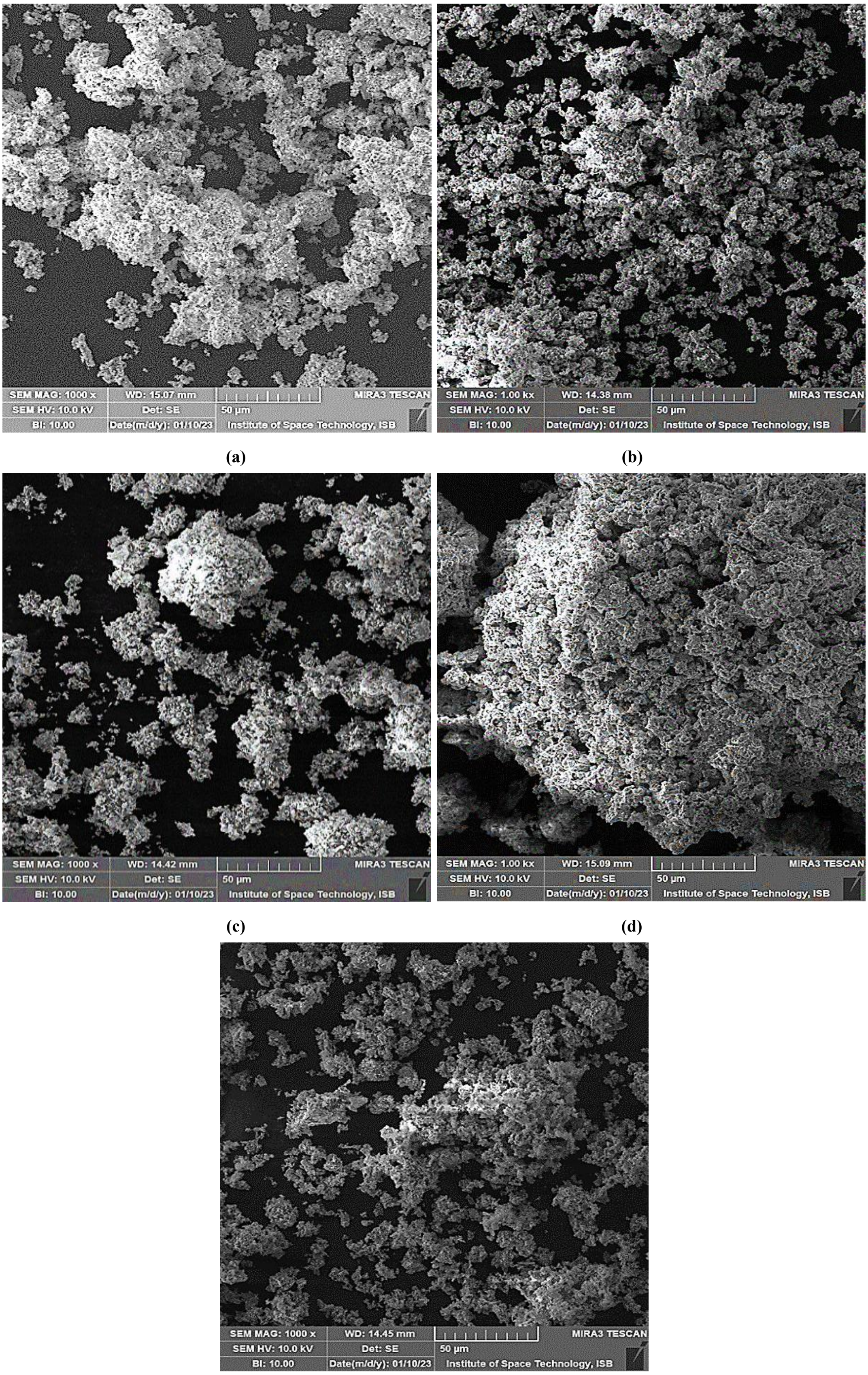

(a) **(b)**

(c) **(d)**

(e)

Figure 2. SEM images of HEO-xC at 50 μm resolution power, **(a)** HEO; **(b)** HEO-5C; **(c)** HEO-10C; **(d)** HEO-15C; **(e)** HEO-20C.

Note: The magnification scale is 50 μm.

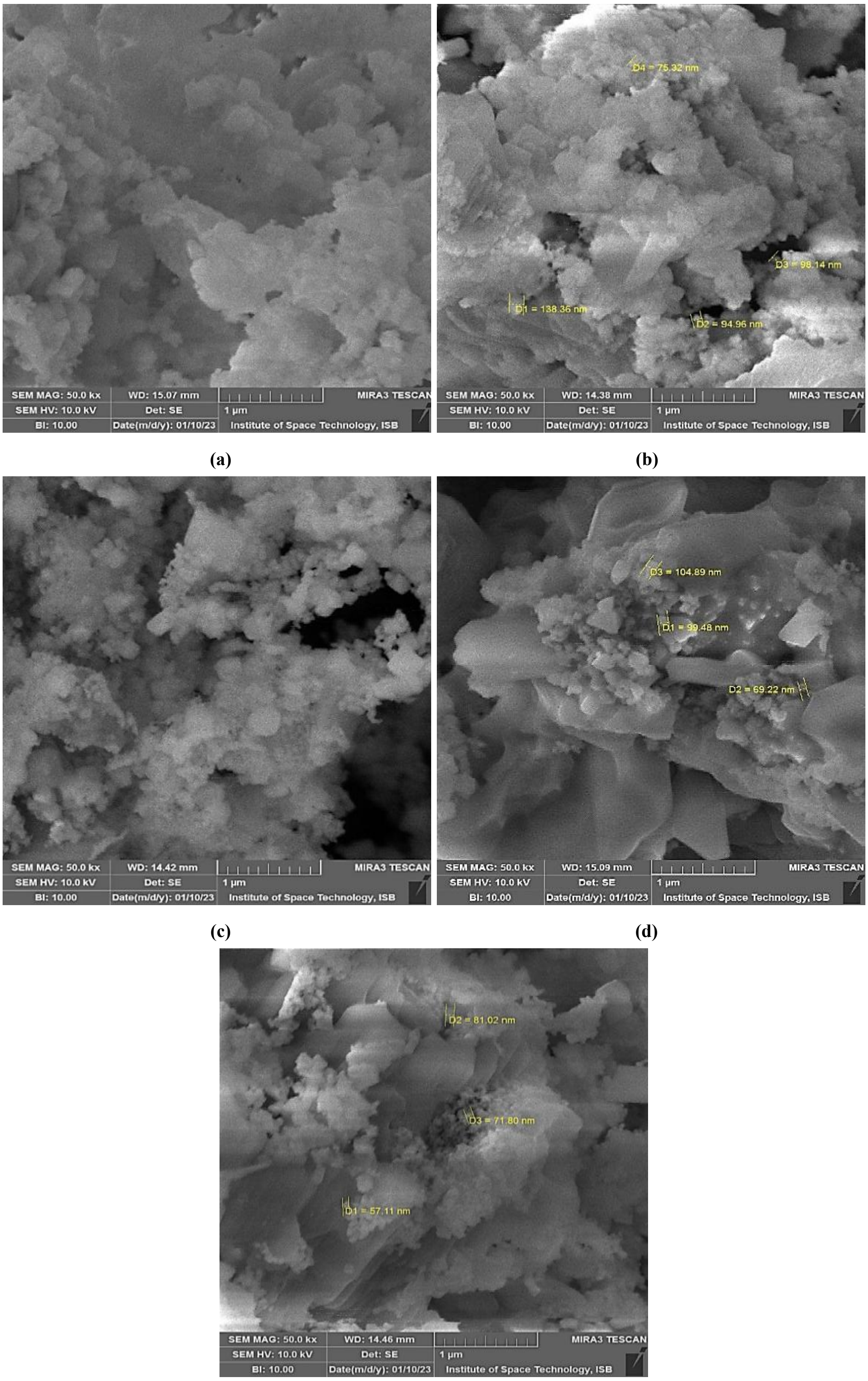

(a) **(b)**

(c) **(d)**

(e)

Figure 3. SEM images of HEO-C at 1 μm resolution power, **(a)** HEO; **(b)** HEO-5C; **(c)** HEO-10C; **(d)** HEO-15C; **(e)** HEO-20C.

Note: The magnification scale is 1 μm; D values measured in **Figure 3** (high magnification) are shown in nanometers (nm).

3.2. Electrochemical studies of HEO-xC towards OER

Electrochemical characterization of the high-entropy oxide/carbon (HEO-xC) materials was conducted using a three-electrode configuration with a Gamry Interface

1000 potentiostat. The setup comprised a modified glassy carbon working electrode, a platinum wire counter electrode, and an Ag/AgCl (3 M KCl) reference electrode. Cyclic voltammetry (CV), linear sweep voltammetry (LSV), and electrochemical impedance spectroscopy (EIS) were employed to evaluate the OER activity and electrochemical performance. Key parameters, including overpotential, Tafel slope, and charge transfer resistance, were derived from the obtained data to quantify the electrocatalytic efficiency and reaction kinetics of the HEO-xC composites [37,38]. The OER activity of the synthesized materials was evaluated via CV in 1 M potassium hydroxide (KOH) electrolyte, both in the absence and presence of 1 M methanol as an additive. The electrochemical measurements were performed using a glassy carbon electrode (GCE), modified with the as-synthesized catalysts, as the working electrode. To assess the reaction kinetics, systematic studies were conducted by varying methanol concentration (to probe its influence on OER activity) and scan rates (to investigate charge transfer dynamics and mass transport effects).

3.2.1. Methanol concentration effect

Methanol was employed as a supporting electrolyte additive in 1 M KOH to investigate its influence on the electron transfer kinetics of the OER. As the methanol concentration increased from 0.25 M to 1 M, a substantial enhancement in peak current density (from μA to mA range) was observed (**Figure 4a**), indicating that methanol facilitates faster electron transfer kinetics at the electrocatalyst surface. **Figure 4b** illustrates the CV response in 1 M KOH + 1 M MeOH. **Figure 4c,d** presents the Reinmuth plot and concentration-dependent response for all modified glassy carbon electrodes (GCEs) in 1 M KOH + 1 M MeOH. Further increasing the methanol concentration to 2 M led to continued peak current enhancement for most catalysts. However, HEO-10C- modified glassy carbon electrode (MGCE) exhibited saturation behavior beyond 1.5 M MeOH, as evidenced by marginal differences in anodic peak current (I_{pa}) between 1.5 M and 1.75 M. This suggests a diffusion-limited region or active site saturation at higher methanol concentrations for this specific composite.

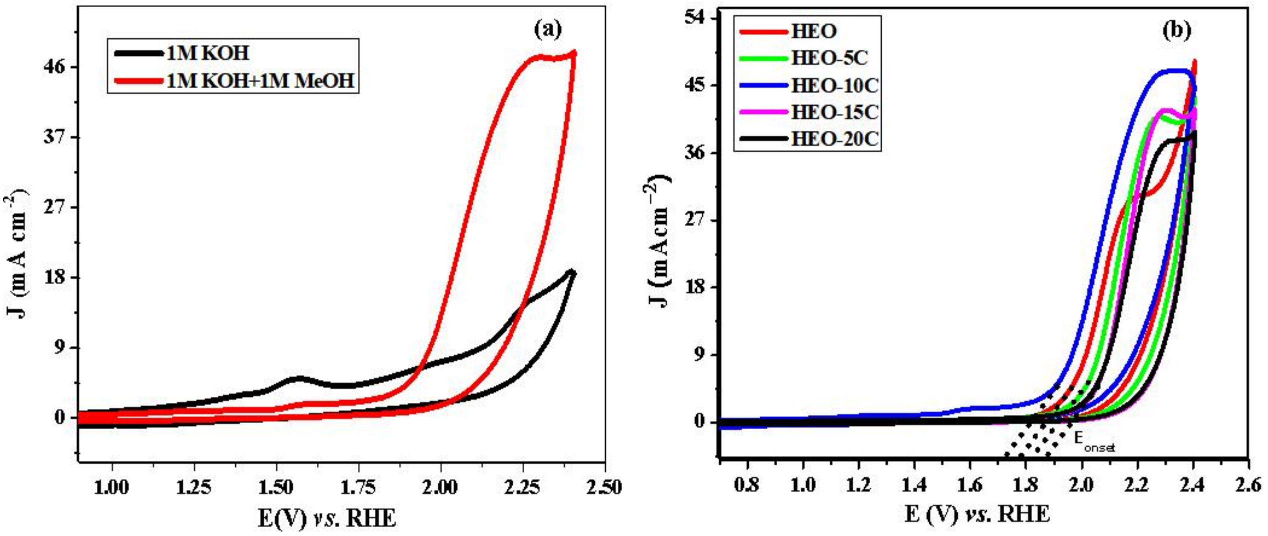

Figure 4. *Cont.*

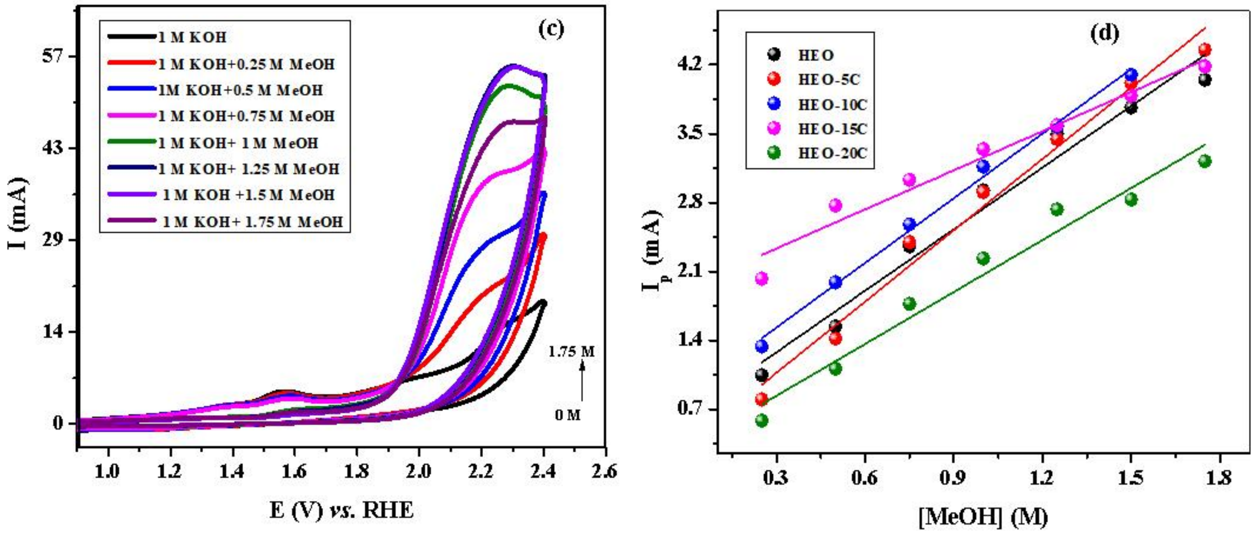

Figure 4. For HEO-10C modified electrode: **(a)** Comparison of CV responses in the (black) absence and presence of methanol (red); **(b)** CV scans of all catalysts modified GC electrode in 1 M KOH+ 1 M MeOH at 100 mV s^{-1}; **(c)**CV response of HEO-10C in 1 M KOH + (0–1.75 M) methanol; **(d)** Reinmuth plot for all MGCE.

The heterogeneous rate constant (k^0) serves as a critical kinetic parameter for evaluating electrocatalytic activity, as it quantifies the intrinsic charge transfer efficiency between the electrode and redox species. The magnitude of k^0 further provides mechanistic insight, distinguishing between reversible ($k^0 > 0.1$ cm/s) and irreversible ($k^0 < 10^{-5}$ cm/s) electrochemical processes. For the as-synthesized materials, k^0 was determined experimentally using the Reinmuth equation [39].

$$I_P = 0.277nFACk^0 \tag{3}$$

The above equation is known as the Reinmuth equation used to calculate the value of k^0, which is given in **Table 2**. In Equation (3), "n" is the number of electrons involved in the reaction, C is the concentration of methanol, A is the active surface area of the working electrode, F is the Faraday's constant, I_P is the anodic peak current, and k^0 is the heterogeneous rate constant.

Table 2. Retrieved OER kinetic parameters for all HEO-xC.

Sample codes	Heterogeneous rate constant $k^0/10^{-4}$ (cms^{-1})	Diffusion constant $D^0/10^{-8}$ (cm^2/s)	Mass transport coefficient $m_T/10^{-4}$ (cm/s)
HEO	3.14	1.25	2.20
HEO-5C	3.37	5.15	4.47
HEO-10C	3.75	8.64	5.80
HEO-15C	3.50	4.84	3.34
HEO-20C	3.20	2.75	3.27

3.2.2. Scan rate effect

The electrocatalytic properties of all MGCEs were evaluated through CV within a potential window of 0 to 1.5 V (vs. RHE) at scan rates ranging from 20 to 100 mV s^{-1} under ambient conditions (**Figure 5a**). Systematic variation of the scan rate revealed enhanced electron transfer kinetics at the electrode-electrolyte interface, as evidenced by increasing peak currents. A linear correlation between the anodic peak current (I_p) and the square root of the scan rate ($\upsilon^{1/2}$) was observed (**Figure 5b**), confirming a diffusion-controlled reaction mechanism. Comparative analysis of all materials demonstrated favorable oxygen evolution reaction (OER) activity across the tested scan rates. The linear I_p vs. $\upsilon^{1/2}$ relationships for all MGCEs further validate the consistent diffusion-limited behavior across the catalyst series. **Figure 5c** presents a comparative analysis of the diffusion coefficient (D^0), heterogeneous rate constant (k^0), and mass transport (m_T) parameters for all MGCEs. These results collectively demonstrate the robust electrocatalytic performance of the synthesized materials.

The diffusion coefficient for an irreversible redox process was determined by using the Randles-Sevcik equation [22,40,41], and it is given as:

$$I_p = (2.99 \times 10^5)\, n\, ((1-\alpha)n_\alpha)^{1/2}\, A\, D^{0\ 1/2}\, C\, \nu^{1/2} \tag{4}$$

Where I_p is anodic peak current in amperes (A), n is the number of electrons involved in the reaction, n_α is the number of electrons involved in the rate-determining step, α is known as the transfer coefficient, A is active surface area of MGCE in cm^2, D^0 is the diffusion coefficient in $cm^2\ s^{-1}$, C is the analyte concentration in mol cm^{-3}, and ν is the scan rate in mV s^{-1}.

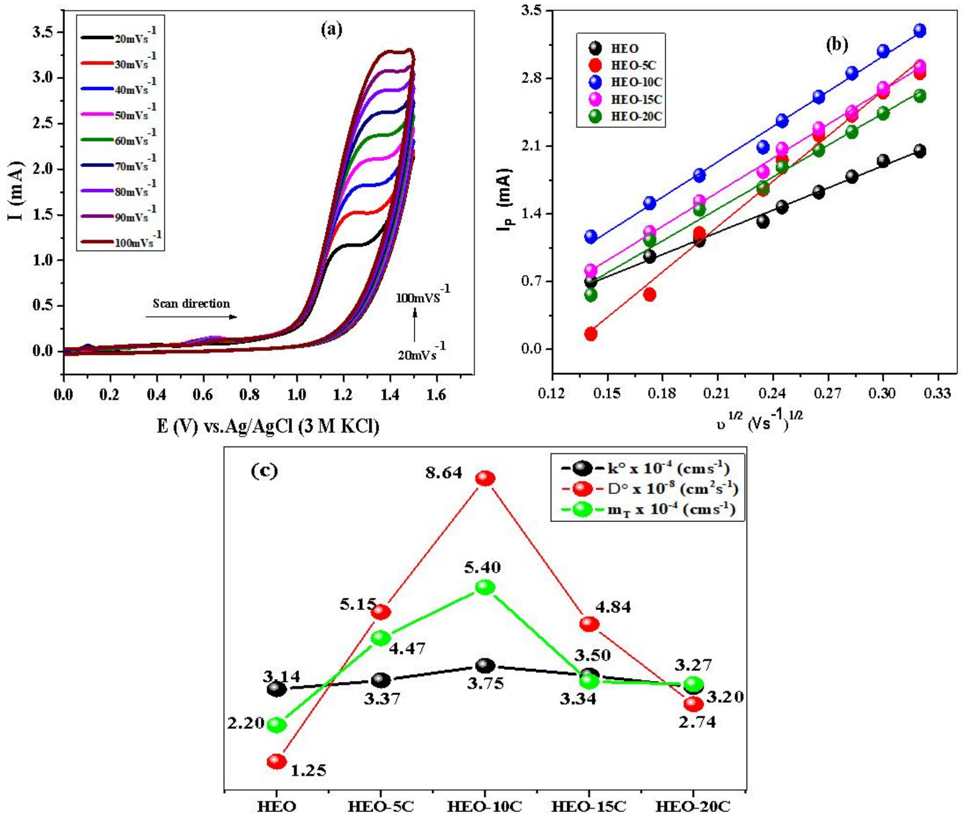

Figure 5. **(a)** Scan rate effect for HEO-10C; **(b)** linear plot of all modified GCE; **(c)** comparison of D^0, k^0, and m_T.

The transfer coefficient (α) for an anodic reaction can be calculated by using Equation (5).

$$E_{pa} - E_{pa/2} = 0.048/(1-\alpha)n \tag{5}$$

The diffusion characteristics of the water oxidation process were quantitatively analyzed by constructing plots of anodic peak current (I_p) versus the square root of scan rate ($\upsilon^{1/2}$). Linear regression of these plots yielded slopes from which the apparent diffusion coefficient (D^o) was calculated using the Randles-Ševčík equation. The observed linear relationships ($R^2 > 0.98$) across all catalyst compositions provide strong evidence that the oxygen evolution reaction (OER) proceeds via a diffusion-controlled mechanism. This conclusion is further supported by the consistent proportionality between peak current enhancement and increasing scan rate, characteristic of mass-transport limited electrochemical processes [42]. The corresponding D^o values are given in **Table 2**, and the maximum value 8.64×10^{-8} $cm^2\ s^{-1}$ was observed by HEO-10C. The mass transport coefficient is calculated by using the formula.

$$m_T = [D^\circ/(RT/F\nu)]^{1/2} \tag{6}$$

The reversibility of any chemical reaction can be identified by a comparison of its k^0 with m_T. If $k^\circ >> m_T$, indicates the reaction is electrochemically reversible, $k^0 << m_T$ indicates the reaction is irreversible. $k^0 \leq 10^{-5}$ cm s^{-1} indicate the EC reaction is irreversible [40]. The values of mass transport coefficients for OER using modified electrodes are given in **Table 2**.

3.2.3. Comparison of peak current values of all modified electrodes

The OER activity of the modified glassy carbon electrodes (MGCEs) was systematically evaluated through cyclic voltammetry in 1 M KOH containing 1 M methanol. As shown in **Figure 6a**, all catalyst compositions exhibited enhanced peak current densities (J) with increasing scan rates (20–100 mV s^{-1}), indicating a combined diffusion- and kinetics-controlled reaction mechanism. Comparative analysis revealed that the HEO-10C composite demonstrated superior electrocatalytic performance, achieving a maximum current density of 47.09 mA cm^{-2}. The improvement over the baseline HEO material (without carbon) suggests that the 10% graphite coating optimally enhances both charge transfer efficiency and active site accessibility. The observed performance hierarchy (HEO-10C > HEO-15C > HEO > HEO-20C > HEO-5C) confirms that while all HEO-xC variants exhibit competent OER activity, the 10% carbon incorporation provides the most favorable balance between electrical conductivity and catalytic site availability.

The catalytic efficiency of the synthesized materials was comprehensively evaluated through multiple electrochemical parameters: onset potential (E_{onset}), Tafel slope (TS), diffusion coefficient (D^o), heterogeneous rate constant (k^0), and overpotential (η). While E_{onset} determination presents challenges due to its operational definition as the potential where charge transfer initiates, it remains a valuable comparative metric for catalytic activity [43]. Tafel analysis provides critical insights into the reaction kinetics and mechanism, with lower TS values indicating superior catalytic performance. Our measurements in 1 M KOH + 1 M MeOH at 100 mV s^{-1} revealed the following activity trend based on TS values: HEO-10C (90 mV dec^{-1}) < HEO-5C (116 mV dec^{-1}) < HEO-15C (123 mV dec^{-1}) < HEO-20C (127 mV dec^{-1}) <

HEO (131 mV dec^{-1}). The optimal performance of HEO-10C, exhibiting the lowest TS, suggests its enhanced charge transfer kinetics and most favorable reaction pathway among the series.

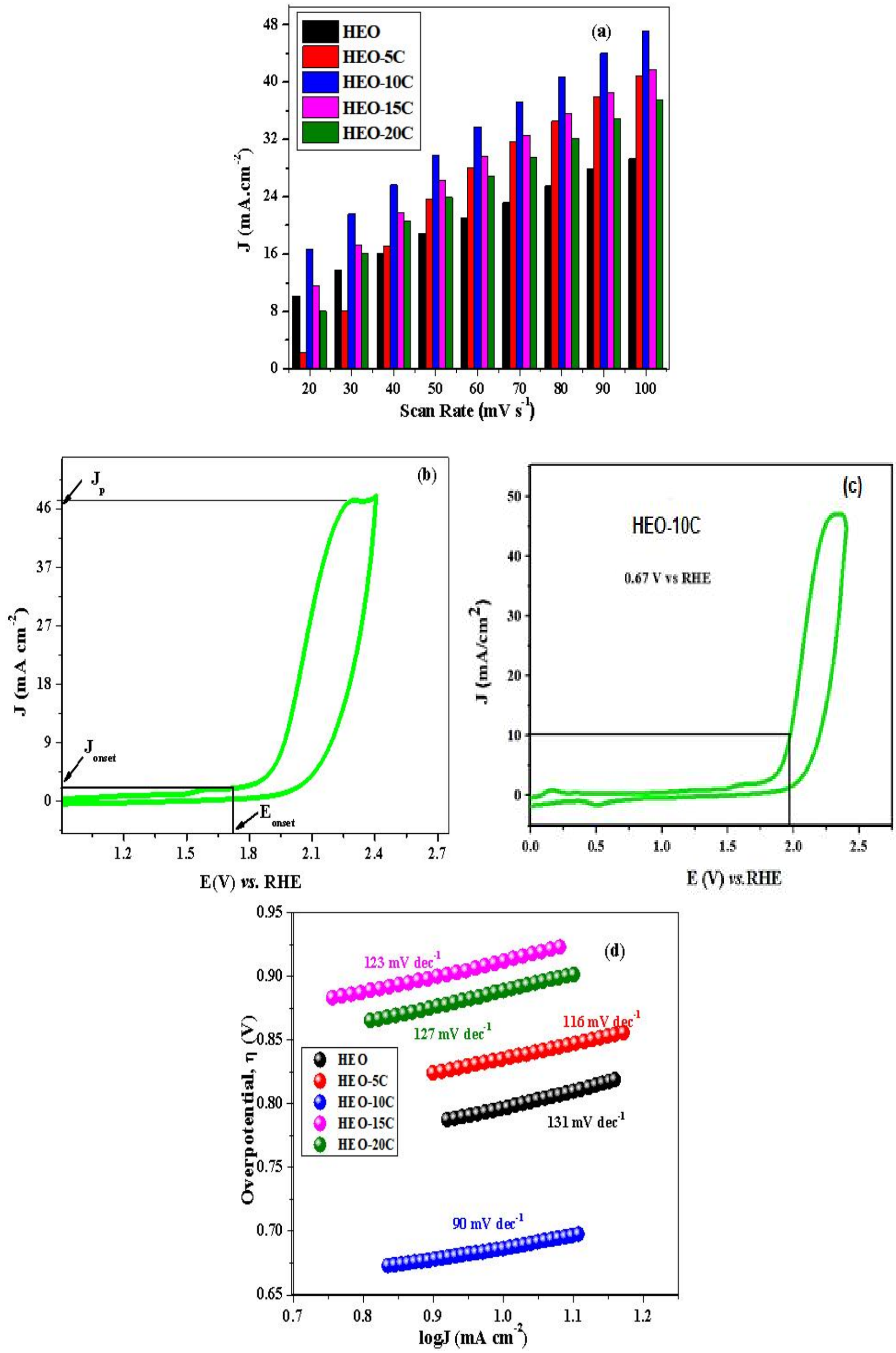

Figure 6. For all MGCE in 1 M KOH plus 1 M MeOH: **(a)** Comparison of peak current density vs. scan rate for water oxidation at all MGCE at a scan rate range of 20–100 mV s^{-1}; **(b)** onset potential; **(c)** CV profile at HEO-10C MGCE indicating overpotential; **(d)** Tafel slope.

The overpotential ($\eta = E - E_{eq}$), representing the additional energy required beyond the thermodynamic potential (Eeq) to drive the reaction at a specific current density, further confirmed this trend. As shown in **Figure 6b,d**, the HEO-10C catalyst demonstrated both the lowest onset potential and the most favorable Tafel characteristics, consistent with its superior catalytic activity. These parameters collectively establish that while all HEO-xC variants show competent catalytic behavior, the 10% carbon incorporation achieves the optimal balance between conductivity and active site availability [40,44].

The Tafel slope serves as a direct indicator of the activation energy barrier, where lower values correspond to more favorable reaction kinetics. As shown in **Figure 6c**, the onset potential (E_{onset}) for HEO-10C was determined from the intersection of the baseline and tangent to the rising current, with the corresponding current density denoted as J_{onset}. We introduce a novel performance metric, J_η, defined as:

$$J_\eta = J_p \text{ (peak current density in KOH + MeOH)} - J_{onset} \tag{7}$$

This parameter quantitatively reflects catalytic efficiency, where larger $J\eta$ values indicate superior performance. The HEO-10C composite demonstrated exceptional characteristics with a maximum J_η (44.59 mA cm^{-2}), highest J_p (47.09 mA cm^{-2}), optimal kinetic parameters (lowest TS = 97 mV dec^{-1}), favorable overpotential (η_{10} = 0.67 V), and low E_{onset} (1.73 V vs. RHE). These results, summarized in **Table 3**, show excellent correlation with fundamental electrochemical parameters (k^0, D_0). The potential values, originally measured versus Ag/AgCl (3 M KCl), were converted to the RHE scale using Equation (7). **Figure 7a** compares η, E_{onset}, and J across all MGCEs, while **Figure 7b** shows a comparison of TS, Jp, and E_{onset}, confirming the superior performance of HEO-10C through multiple evaluation criteria [45].

$$\mathbf{E}_{RHE}(V) = E_{Ag/AgCl} + 0.197 + 0.059\,pH \tag{8}$$

3.2.4. Electrochemical impedance spectroscopy (EIS)

Electrochemical impedance spectroscopy (EIS) was employed to characterize the charge transfer properties and interfacial behavior of the HEO-modified glassy carbon electrodes in both 1 M KOH and KOH/methanol solutions. The impedance data were modeled using an equivalent circuit incorporating solution resistance (R_s), charge transfer resistance (R_{ct}), constant phase element (Q), and pseudo capacitance (C) [46,47]. Nyquist plots, presenting the real (Z') versus imaginary (Z'') impedance components, were analyzed using a CPE-modified diffusion model to extract quantitative parameters. Notably, the HEO-10C composite exhibited superior charge transfer characteristics, demonstrating the lowest R_t values among all compositions - decreasing significantly from 292.9 Ω in pure KOH to 66.8 Ω in methanol-containing electrolyte. This substantial reduction in charge transfer resistance (~77% decrease) clearly indicates methanol's role in facilitating interfacial electron transfer processes. The complete set of fitted electrical parameters for all samples is presented in **Table 4**, with corresponding Nyquist plots shown in **Figure 8**. These EIS results correlate well with the observed enhancement in catalytic activity, particularly for the HEO-10C formulation, as evidenced by its superior performance in voltammetric studies.

Table 3. OER performance parameters for HEO-xC.

Samples	J_p (mA/cm^2)	J_{onset} (mA/cm^2)	$J\eta = (Jp{-}J_{onset})$ (mA/cm^2)	E_{onset} vs. RHE (V)	η_{10} vs. RHE (V)	TS (mV dec^{-1})
HEO	29.28	1.39	27.89	1.87	0.80	131
HEO-5C	40.85	1.49	39.36	1.92	0.86	116
HEO-10C	47.09	2.50	44.59	1.80	0.67	90
HEO-15C	41.71	1.13	40.58	1.92	0.87	123
HEO-20C	37.43	1.19	36.24	1.92	0.86	127

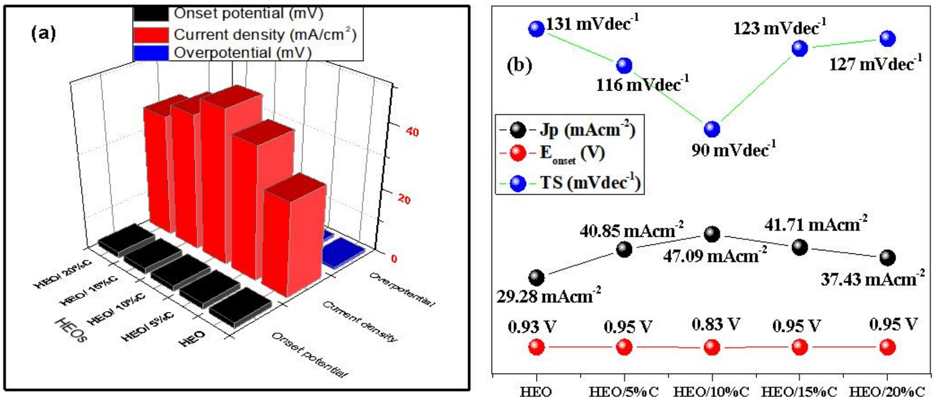

Figure 7. (a,b) Comparison of OER performance parameters of all modified GCE in 1M KOH + 1M MeOH at 100 mV s^{-1}.

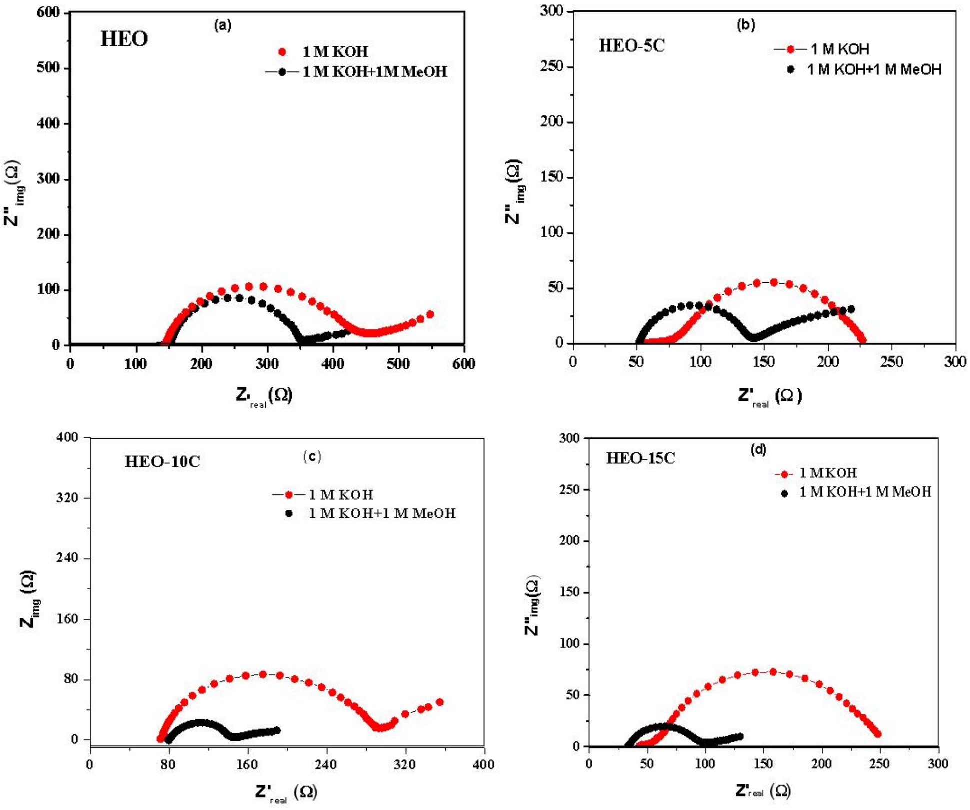

Figure 8. *Cont.*

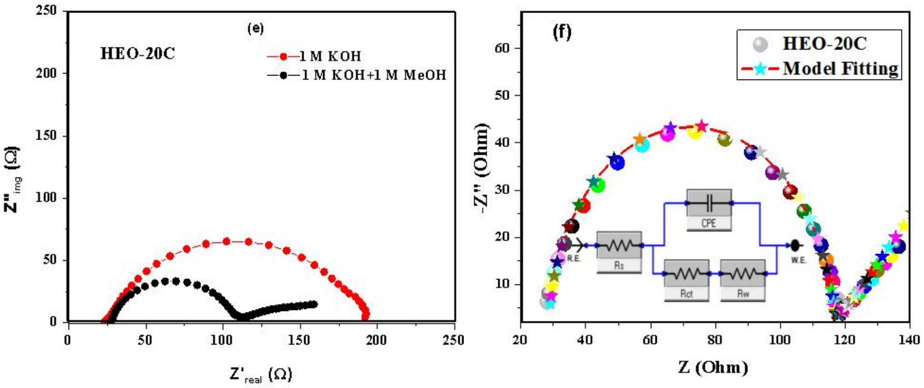

Figure 8. Nyquist plots of **(a)** HEO; **(b)** HEO-5C; **(c)** HEO-10C; **(d)** HEO-15C; **(e)** HEO-20C modified GCE in 1 M KOH (red) and 1 M KOH + 1 M MeOH (black); **(f)** EIS circuit diagram and model fitting of HEO-20C in 1 M KOH + 1 M MeOH.

Table 4. EC data acquired from Nyquist plots for OER on HEO-xC-modified GCE in 1M KOH and 1M KOH + 1M MeOH.

	EC parameters	**HEO**	**HEO-5C**	**HEO-10C**	**HEO-15C**	**HEO-20C**
1M KOH	R_s (Ω)	142.99	80.99	72.07	54.60	24.62
	R_{CT} (Ω)	293.71	145.78	220.24	194.09	167.67
	CPE (μF)	3.8	2.6	5.0	8.2	4.0
	α	0.95	0.92	0.83	0.87	0.88
	W_d (mΩ)	10.2	17.2	4.2	16.9	5.8
1M KOH + 1M MeOH	R_s (Ω)	150.70	51.25	78.11	33.45	27.48
	R_{CT} (Ω)	199.38	90.34	67.13	68.52	84.32
	CPE (μF)	3.6	3.8	7.5	13.6	7.3
	α	0.86	0.84	0.82	0.70	0.78
	W_d (mΩ)	24.9	15.6	3.0	13.5	10.6

4. Conclusion

We successfully synthesized aluminum-rich HEOs with composition $[Al_{35}(CdCrFeMgMn)_{65}]_3O_4$ and their graphite-coated derivatives (5−20% C) through a combined sol-gel and ball-milling approach. Structural characterization revealed a well-defined cubic spinel phase (XRD) with nanocrystalline domains (20−30 nm) and characteristic metal-oxygen vibrational modes (FTIR), confirming phase purity. Microscopic analysis (SEM/EDX) demonstrated a highly porous, agglomerated morphology with uniform elemental distribution. Electrochemical evaluation in alkaline methanol media (1 M KOH + 1 M MeOH) revealed exceptional oxygen evolution reaction (OER) activity across all compositions, with the 10% carbon variant exhibiting optimal performance: a diffusion coefficient of 8.64×10^{-8} cm^2 s^{-1}, heterogeneous electron transfer rate of 3.75×10^{-4} cm s^{-1}, minimal charge transfer resistance (66.8 Ω), and favorable Tafel kinetics (90 mV dec^{-1}). These superior metrics, coupled with the observed diffusion-controlled mechanism and excellent mass transport properties, establish these HEO-xC composites—particularly the 10% carbon formulation—as highly promising electrocatalysts for water splitting applications and related energy conversion technologies.

Author contributions: Conceptualization, JA, AH (Amina Hana) and MY; methodology, SA, AH (Akbar Hussain), MA, TMB and NKJ; validation, SA, AH (Akbar Hussain), MA and TMB; formal analysis, SA, AH (Akbar Hussain), MA and TMB; investigation, SA, AH (Akbar Hussain), MA and TMB; experimental access, JA, AH (Amina Hana) and MY; writing—original draft preparation, SA, AH (Akbar Hussain), MA, TMB and NKJ; writing—review and editing, SA, AH (Akbar Hussain), MA, TMB, BHUR, SK and NKJ; supervision, NKJ. All authors have read and agreed to the published version of the manuscript.

Funding: This work was supported by Quaid-i-Azam University, Islamabad, for the provision of the lab facilities and the Higher Education Commission of Pakistan under project No. 14-4768.

Institutional review board statement: Not applicable.

Informed consent statement: Not applicable.

Data availability statement: All the datasets analyzed during the current study are available from the corresponding author on reasonable request.

Conflict of interest: The authors declare that the research was conducted in the absence of any commercial or financial relationships that could be construed as a potential conflict of interest.

AI use statement: During the manuscript writing, AI tools (DeepSeek and Quilbot) were used only to improve scientific writing and better comprehension. After using the tool, the authors reviewed the manuscript and take full responsibility for the content of the published articles.

References

1. Hassan A, Ilyas SZ, Jalil A, et al. Monetization of the environmental damage caused by fossil fuels. Environmental Science and Pollution Research. 2021; 28(17): 21204–21211. doi: 10.1007/s11356-020-12205-w
2. Ajewole T, Olabode O, Ariyo F, et al. Conceptual perspective of renewable energy resources. In: Adaptive Power Quality for Power Management Units Using Smart Technologies. CRC Press; 2023. pp. 67–103. doi: 10.1201/9781003436461-3
3. Shahzad A, Jiang HJ, Aguey-Zinsou KF. Unitized regenerative fuel cells: Fundamental challenges and advancements. Renewable and Sustainable Energy Reviews. 2025; 215: 115631. doi: 10.1016/j.rser.2025.115631
4. Abbas Q, Mirzaeian M, Hunt MRC, et al. Current State and Future Prospects for Electrochemical Energy Storage and Conversion Systems. Energies. 2020; 13(21): 5847. doi: 10.3390/en13215847
5. Ang TZ, Salem M, Kamarol M, et al. A comprehensive study of renewable energy sources: Classifications, challenges and suggestions. Energy Strategy Reviews. 2022; 43: 100939. doi: 10.1016/j.esr.2022.100939
6. Najjar YSH. Hydrogen safety: The road toward green technology. International Journal of Hydrogen Energy. 2013; 38(25): 10716–10728. doi: 10.1016/j.ijhydene.2013.05.126
7. Nandihalli N. Microwave-driven synthesis and modification of nanocarbons and hybrids in liquid and solid phases. Journal of Energy Storage. 2025; 111: 115315. doi: 10.1016/j.est.2025.115315
8. Xiong B, Chen L, Shi J. Anion-Containing Noble-Metal-Free Bifunctional Electrocatalysts for Overall Water Splitting. ACS Catalysis. 2018; 8(4): 3688–3707. doi: 10.1021/acscatal.7b04286
9. Huo WY, Wang SQ, Zhu WH, et al. Recent progress on high-entropy materials for electrocatalytic water splitting applications. Tungsten. 2021; 3(2): 161–180. doi: 10.1007/s42864-021-00084-8
10. Pasupathi A, Madhu R, Govindarajan S, et al. Scalable Fabrication of Bifunctional HEO Electrodes via Solution

Plasma Spraying: Tailoring Thickness and Surface Features for Efficient Water Splitting. Energy & Fuels. 2025; 39(50): 23805–23819. doi: 10.1021/acs.energyfuels.5c04755

11. Pasupathi A, Kandasamy P, Dharman RK, et al. A facile approach to deposit high performance electrocatalyst high entropy oxide coatings using a novel plasma spray route for efficient water splitting in an alkaline medium. Sustainable Energy & Fuels. 2025; 9(12): 3323–3334. doi: 10.1039/D5SE00479A
12. Asim M, Hussain A, Khan S, et al. Sol-Gel Synthesized High Entropy Metal Oxides as High-Performance Catalysts for Electrochemical Water Oxidation. Molecules. 2022; 27(18): 5951. doi: 10.3390/molecules27185951
13. Rost CM, Sachet E, Borman T, et al. Entropy-stabilized oxides. Nature Communications. 2015; 6(1): 8485. doi: 10.1038/ncomms9485
14. Dippo OF, Vecchio KS. A universal configurational entropy metric for high-entropy materials. Scripta Materialia. 2021; 201: 113974. doi: 10.1016/j.scriptamat.2021.113974
15. Liang J, Liu J, Wang H, et al. Synthesis of Ultrathin High-Entropy Oxides with Phase Controllability. Journal of the American Chemical Society. 2024; 146(11): 7118–7123. doi: 10.1021/jacs.3c10868
16. Goudar JA, Thrinethra SN, Chapi S, et al. Temperature-dependent electrical conductivity and dielectric response of Co-doped $MnFe_2O_4$spinel ferrite. Ionics. 2025; 31(11): 12413–12439. doi: 10.1007/s11581-025-06699-y
17. Asim M, Hussain A, Kanwal S, et al. Unveiling the potential of rock-salt type high entropy oxides synthesized by green microwave irradiation method for excellent oxygen evolution reaction. Journal of Alloys and Compounds. 2025; 1016: 178967. doi: 10.1016/j.jallcom.2025.178967
18. He H, Kou P, Zhang Z, et al. Coupling high entropy oxide with hollow carbon spheres by rapid microwave solvothermal strategy for boosting oxygen evolution reaction. Journal of Colloid and Interface Science. 2024; 653: 179–188. doi: 10.1016/j.jcis.2023.09.063
19. Yang X, Liping S, Qiang L, et al. Co-prosperity of electrocatalytic activity and stability in high entropy spinel $(Cr_{0.2}Mn_{0.2}Fe_{0.2}Ni_{0.2}Zn_{0.2})_3O_4$ for the oxygen evolution reaction. Journal of Materials Chemistry A. 2022; 10(34): 17633–17641. doi: 10.1039/D2TA01376B
20. Wang D, Liu Z, Du S, et al. Low-temperature synthesis of small-sized high-entropy oxides for water oxidation. Journal of Materials Chemistry A. 2019; 7(42): 24211–24216. doi: 10.1039/C9TA08740K
21. Zhang Y, Dai W, Zhang P, et al. In-situ electrochemical tuning of $(CoNiMnZnFe)_3O_{3.2}$ high-entropy oxide for efficient oxygen evolution reactions. Journal of Alloys and Compounds. 2021; 868: 159064. doi: 10.1016/j.jallcom.2021.159064
22. Asim M, Hussain A, Kanwal S, et al. Rapid microwave synthesis of medium and high entropy oxides for outstanding oxygen evolution reaction performance. Materials Advances. 2024; 5(21): 8490–8504. doi: 10.1039/D4MA00667D
23. Kante MV, Weber ML, Ni S, et al. A High-Entropy Oxide as High-Activity Electrocatalyst for Water Oxidation. ACS Nano. 2023; 17(6): 5329–5339. doi: 10.1021/acsnano.2c08096
24. Liu Y, Ye C, Chen L, et al. High Entropy-Driven Role of Oxygen Vacancies for Water Oxidation. Advanced Functional Materials. 2024; 34(25): 2314820. doi: 10.1002/adfm.202314820
25. Nandihalli N. A Review of Nanocarbon-Based Anode Materials for Lithium-Ion Batteries. Crystals. 2024; 14(9): 800. doi: 10.3390/cryst14090800
26. Chiu CT, Teng YJ, Dai BH, et al. Novel high-entropy ceramic/carbon composite materials for the decomposition of organic pollutants. Materials Chemistry and Physics. 2022; 275: 125274. doi: 10.1016/j.matchemphys.2021.125274
27. He X, Zhang Z, Jiang X, et al. Carbon cloth supporting $(CrMnFeCoCu)_3O_4$ high entropy oxide as electrocatalyst for efficient oxygen evolution reactions. Journal of Alloys and Compounds. 2024; 1004: 175874. doi: 10.1016/j.jallcom.2024.175874
28. Wang Q, Chen J, Feng B, et al. Engineering metal-oxide interfacial structures over $(FeCoNiCrMo)_3O_4$/CNT spinel high entropy oxide for efficient overall water splitting. International Journal of Hydrogen Energy. 2025; 128: 656–664. doi: 10.1016/j.ijhydene.2025.04.276
29. Mao A, Quan F, Xiang HZ, et al. Facile synthesis and ferrimagnetic property of spinel $(CoCrFeMnNi)_3O_4$ high-entropy oxide nanocrystalline powder. Journal of Molecular Structure. 2019; 1194: 11–18. doi: 10.1016/j.molstruc.2019.05.073
30. Mourdikoudis S, Pallares RM, Thanh NTK. Characterization techniques for nanoparticles: Comparison and complementarity upon studying nanoparticle properties. Nanoscale. 2018; 10(27): 12871–12934. doi: 10.1039/C8NR02278J
31. Canales C, Gidi L, Ramírez G. Electrochemical Activity of Modified Glassy Carbon Electrodes with Covalent Bonds Towards Molecular Oxygen Reduction. International Journal of Electrochemical Science. 2015; 10(2): 1684–1695.

doi: 10.1016/S1452-3981(23)05103-9

32. Saghir AV, Beidokhti SM, Khaki JV, et al. One-step synthesis of single-phase (Co, Mg, Ni, Cu, Zn) O High entropy oxide nanoparticles through SCS procedure: Thermodynamics and experimental evaluation. Journal of the European Ceramic Society. 2021; 41(1): 563–579. doi: 10.1016/j.jeurceramsoc.2020.08.044
33. Gaffney JS, Marley NA, Jones DE. Fourier Transform Infrared (FTIR) Spectroscopy. In: Characterization of Materials. Wiley; 2012. pp. 1–33. doi: 10.1002/0471266965.com107.pub2
34. Dong Q, Hong M, Gao J, et al. Rapid Synthesis of High-Entropy Oxide Microparticles. Small. 2022; 18(11): 2104761. doi: 10.1002/smll.202104761
35. Mallesh S, Noh JS, Nam YW. Structure and magnetic properties of $(Mg_{1/6}Zn_{1/6}Mn_{1/6}Co_{1/6}Ni_{1/6}Fe_{1/6})_3O_4$ nanocrystalline high-entropy oxide synthesized using a sol-gel auto combustion approach. Journal of Magnetism and Magnetic Materials. 2022; 564: 170108. doi: 10.1016/j.jmmm.2022.170108
36. Nuspl M, Wegscheider W, Angeli J, et al. Qualitative and quantitative determination of micro-inclusions by automated SEM/EDX analysis. Analytical and Bioanalytical Chemistry. 2004; 379(4). doi: 10.1007/s00216-004-2528-y
37. Anantharaj S, Ede SR, Karthick K, et al. Precision and correctness in the evaluation of electrocatalytic water splitting: revisiting activity parameters with a critical assessment. Energy & Environmental Science. 2018; 11(4): 744–771. doi: 10.1039/C7EE03457A
38. Butt TM, Janjua NK, Mujtaba A, et al. B-Site Doping in Lanthanum Cerate Nanomaterials for Water Electrocatalysis. Journal of The Electrochemical Society. 2020; 167(2): 026503. doi: 10.1149/1945-7111/ab63c0
39. Butt TM, Ullah A, Janjua NK. Electrokinetic analysis of water oxidation on alumina supported silver oxide nanopowders. Journal of Electroanalytical Chemistry. 2022; 907: 116053. doi: 10.1016/j.jelechem.2022.116053
40. Bard AJ, Faulkner LR, White HS. Electrochemical Methods: Fundamentals and Applications. John Wiley & Sons; 2022.
41. Hussain A, Asim M, Samanci M, et al. Oxygen evolution reaction activity of carbon aerogel supported Pd–Ni–Al catalysts synthesized by microwave irradiation method. International Journal of Hydrogen Energy. 2024; 81: 93–109. doi: 10.1016/j.ijhydene.2024.07.287
42. Karmakar A, Nagappan S, Das A, et al. Exploring the linear relationship between potential dynamics and interfacial capacitance: Implications for enhancing the turnover frequency in electrochemical water splitting. Journal of Materials Chemistry A. 2023; 11(29): 15635–15642. doi: 10.1039/D3TA02540C
43. Holewinski A, Linic S. Elementary Mechanisms in Electrocatalysis: Revisiting the ORR Tafel Slope. Journal of The Electrochemical Society. 2012; 159(11): H864–H870. doi: 10.1149/2.022211jes
44. Liang Q, Brocks G, Bieberle-Hütter A. Oxygen evolution reaction (OER) mechanism under alkaline and acidic conditions. Journal of Physics: Energy. 2021; 3(2): 026001. doi: 10.1088/2515-7655/abdc85
45. Pan L, Kim JH, Mayer MT, et al. Boosting the performance of Cu_2O photocathodes for unassisted solar water splitting devices. Nature Catalysis. 2018; 1(6): 412–420. doi: 10.1038/s41929-018-0077-6
46. Anantharaj S, Noda S. Appropriate Use of Electrochemical Impedance Spectroscopy in Water Splitting Electrocatalysis. ChemElectroChem. 2020; 7(10): 2297–2308. doi: 10.1002/celc.202000515
47. Patil B, Martinez-Lázaro A, Escalona-Villalpando R, et al. Electrochemical Water Splitting. In: Nanochemistry. CRC Press; 2023. pp. 378–395. doi: 10.1201/9781003081944-16